

# From 2D STXM to 3D Imaging: Soft X-ray Laminography of Thin Specimens

Katharina Witte,<sup>\*,†</sup> Andreas Späth,<sup>‡</sup> Simone Finizio,<sup>†</sup> Claire Donnelly,<sup>¶</sup>  
Benjamin Watts,<sup>†</sup> Blagoj Sarafimov,<sup>†</sup> Michal Odstrcil,<sup>†,§</sup> Manuel  
Guizar-Sicairos,<sup>†</sup> Mirko Holler,<sup>†</sup> Rainer H. Fink,<sup>‡</sup> and Jörg Raabe<sup>\*,†</sup>

<sup>†</sup>*Swiss Light Source, Paul Scherrer Institut, Forschungsstrasse 111, 5232 Villigen,  
Switzerland*

<sup>‡</sup>*Department Chemie und Pharmazie, Physikalische Chemie,  
Friedrich-Alexander-Universität Erlangen-Nürnberg, Egerlandstrasse 3, 91058 Erlangen,  
Germany*

<sup>¶</sup>*Cavendish Laboratory, University of Cambridge, JJ Thomson Ave, Cambridge, CB3 0HE,  
United Kingdom*

<sup>§</sup>*Current address: Carl Zeiss SMT GmbH, Rudolf-Eber-Strasse 2, 73447 Oberkochen,  
Germany*

E-mail: [katharina.witte@psi.ch](mailto:katharina.witte@psi.ch); [joerg.raabe@psi.ch](mailto:joerg.raabe@psi.ch)

## Abstract

X-ray tomography has become an indispensable tool for studying complex 3D interior structures with high spatial resolution. 3D imaging using soft X-rays offers powerful contrast mechanisms, but has seen limited success with tomography due to the restrictions imposed by the much lower energy of the probe beam. The generalized geometry of laminography, characterized by a tilted axis of rotation, provides nm-scale 3D resolution for the investigation of extended (mm range) but thin ( $\mu\text{m}$  to

nm) samples that are well suited to soft X-ray studies. This work reports on the implementation of soft X-ray laminography (SoXL) at the scanning transmission X-ray spectromicroscope of the PoLLux beamline at the Swiss Light Source, Paul Scherrer Institut, which enables 3D imaging of extended specimens from 270 eV to 1500 eV. Soft X-ray imaging provides contrast mechanisms for both chemical sensitivity to molecular bonds and oxidation states and magnetic dichroism due to the much stronger attenuation of X-rays in this energy range. The presented examples of applications range from functionalized nanomaterials to biological photonic crystals and sophisticated nanostructured magnetic domain patterns, thus illustrating the wide fields of research that can benefit from SoXL.

**Keywords:** 3D imaging, soft X-rays, laminography, flat and extended specimens, X-ray microscopy

Three-dimensional (3D) imaging techniques using X-ray radiation provide access to the inner architecture of complex objects in an almost non-destructive way, and thus enable further understanding of the relationship between structure and function. Current fields of research ranging from condensed matter physics to biomedical applications<sup>1</sup> and cultural heritage<sup>2</sup> benefit from the use of highly brilliant synchrotron radiation and the development of sophisticated 3D imaging methods such as ptychographic X-ray computed tomography (PXCT)<sup>3,4</sup> or X-ray phase contrast tomographic microscopy.<sup>5</sup> These methods provide nm-depth resolution and in case of phase contrast tomography faster scanning times allow for the possibility to investigate dynamic processes in three dimensions.<sup>6,7</sup>

The tomographic techniques mentioned so far typically use hard X-rays with a photon energy above 5 keV. The use of hard X-rays is advantageous in case of bulk and thicker samples but nevertheless, tomography-based 3D imaging is restricted in the case of extended, planar samples, suffers from increasing material thickness during sample rotation. In the latter case, this results in the so-called "missing wedge" artifact, leading to inaccessible information in

the Fourier space, which makes a meaningful reconstruction of the object more challenging. Furthermore, the risk of collision during rotation is a crucial factor to consider in tomography for such extended samples, limiting the maximum sample size.

In contrast, 3D imaging using soft X-ray tomography<sup>8-11</sup> and concepts combining soft X-ray ptychography and tomography<sup>12,13</sup> are still relatively underused. Scientific questions using these techniques are focusing on research concerning polymer-based materials,<sup>9,14</sup> reaction processes in novel battery and fuel cells concepts<sup>15-17</sup> and soft bio-organic tissue.<sup>18,19</sup> However, in case of the investigation of extended but thin specimens providing a thickness in the  $\mu\text{m}$  to nm-range, soft X-rays ( $E < 1 \text{ keV}$ ) are favored due to their lower penetration depth compared to hard X-rays. Soft X-ray radiation offers further decisive advantages though, as it is sensitive to chemical bonds and oxidation states. Furthermore, the magnetic state of transition metal-based ferromagnetic materials can be investigated by tuning the X-ray energy to the L-absorption edges, which exhibits magnetic contrast up to 30% thanks to the X-ray magnetic circular dichroism (XMCD) effect. These characteristics make soft X-rays the probe of choice to investigate for various kind of microstructured, flat and thin specimen.

The more generalized geometry of laminography,<sup>20-22</sup> in which the axis of rotation is no longer perpendicular to the incident X-ray beam, has proven to be particularly suitable for the investigation of extended, flat objects. In contrast to tomography it does not require the preparation of free-standing samples, that are accessible to the radiation from all directions and ideally cylindrically shaped. Recent advances using hard X-rays allowed laminography to reach sub-20 nm resolution.<sup>23</sup>

The combination of soft X-ray radiation and 3D laminographic imaging has the unique potential of bridging the gap between the investigation of elaborate nanostructured thin film samples with nm-depth resolution and the advantages provided by the characteristic properties of soft X-ray radiation. As a result, Soft X-ray Laminography (SoXL) provides new insights into the interior structure and 3D composition of complex sample systems on the

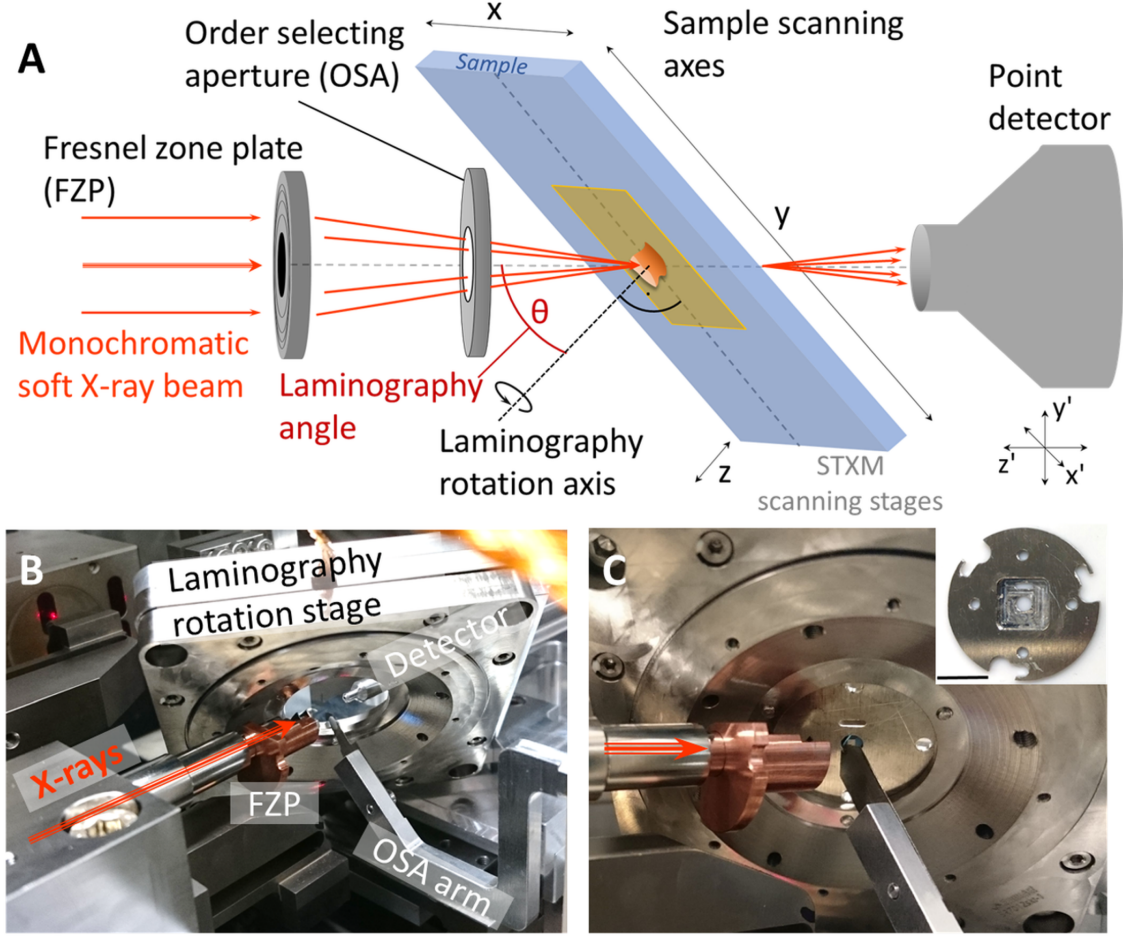


Figure 1: Soft X-ray Laminography (SoXL) at the PolLux beamline. (A) Schematic illustration of the imaging geometry, in which  $xyz$  denotes the sample coordinate system and  $(xyz)'$  denotes the X-ray microscope coordinate system. (B) Photography of the implemented SoXL rotation stage (without sample) on top of the STXM scanning stages. (C) Zoom on the sample position in the SoXL setup with a mounted  $\text{Si}_3\text{N}_4$  membrane on a conventional sample plate (inset, scale bar: 1 cm).

micro- to nanometer scale.

This work reports on SoXL and the new instrumentation for realizing this new technique installed at the PolLux beamline (X07DA) of the Swiss Light Source, Paul Scherrer Institut (PSI), Switzerland. This bending magnet beamline provides soft X-ray radiation in the spectral range between 270 and 1600 eV<sup>24,25</sup> and operates a Scanning Transmission X-ray Microscope (STXM). A detailed description of the instrument can be found elsewhere.<sup>25</sup> For the scope of this letter, the operating principle of STXM can be summarized as follows: The



monochromatic X-ray beam is focused by a Fresnel zone plate (FZP) to a spot diameter of a few tens of nanometers. The first diffraction order light of the FZP is selected by an aperture (order selecting aperture, OSA) to separate it from the directly transmitted (zero-order) light and the higher diffraction orders. The sample is positioned in the focal spot and the transmitted radiation is detected using a point detector while raster-scanning the sample. This enables spatial and spectroscopic information at the same time. Depending on the selected photon energy, the entrance and exit slit settings and the FZP parameters, a spatial resolution  $\Delta x < 10$  nm can be achieved<sup>26</sup> but most commonly,  $\Delta x$  is usually chosen to be between 30 and 40 nm. In the following, the new SoXL-instrumentation will be described and three case studies will present possible applications for SoXL, followed by a discussion of future perspectives using SoXL in combination with time-resolved setups and ptychographic techniques.

In order to realize SoXL in the existing STXM setup, a customized in-vacuo rotation piezo-stage (SmarAct GmbH, SR-7021-S-HVK-TI) was mounted on top of the STXM-translation stages, denoted as  $(xyz)$ '-coordinate system. A schematic of all STXM-scanning stages including the SoXL rotation stage can be found in Figure S1 of the Supplementary Information (SI). The rotation axis, coincident with the sample surface normal, points downwards to increase the available space for the STXM focusing elements as can be seen in Figure 1. Two configurations are implemented with a laminography angle  $\theta$ , i. e. the angle between the incident X-ray beam and the axis of rotation, of either  $45^\circ$  or  $60^\circ$ .

A free and flexible selection of the area of interest on the sample is possible within a scanning range of  $1000 \times 1000 \mu\text{m}^2$ , only restricted by the available travel range of the scanning stages and the measurement time. The sample thickness is however limited by two factors. On the one hand, the attenuation length of soft X-rays (270 - 1600 eV) determines the maximum amount of sample material and lies in the range of a few hundred nm to one or two  $\mu\text{m}$

(ignoring voids). On the other hand, the depth of focus (DOF),

$$DOF = \pm \frac{2(\Delta r_N)^2}{\lambda} = \pm \frac{2E(\Delta r_N)^2}{hc} \quad (1)$$

which is defined by the used FZP (outermost zone width  $\Delta r_N$ ), the Planck constant  $h$ , the vacuum speed of light  $c$  and the photon energy  $E$ , limits the accessible information depth unless focal stack measurements are acquired.<sup>27</sup> In order to ensure the highest possible resolution in the subsequent 3D reconstruction, the maximum sample thickness should be less than the DOF, which is usually in the range of a few  $\mu\text{m}$ . Note that for the SoXL-geometry the effective sample thickness  $d_{eff}$  is increased by  $d/\cos\theta$  ( $d$ : nominal sample thickness), resulting a factor of 1.4 for  $\theta=45^\circ$  and a factor of 2 for  $\theta=60^\circ$ . This has to be considered when selecting and preparing a sample for SoXL. The sample is usually deposited on an X-ray transparent  $\text{Si}_3\text{N}_4$  membrane or a transmission electron microscopy (TEM)-grid and placed at the center of the sample plate, which is depicted in the inset of Figure 1C. Tailored printed circuit boards (PCB) for applying electrical excitations to a sample are further available (see Figure S3).

The sample positioning in  $(xy)'$ -direction can be achieved with nm-precision thanks to an optical laser interferometer system.<sup>25</sup> By implementing an additional laser on the FZP-stage and a reflection mirror on the sample stage, the system has been extended by the  $z'$ -axis parallel to the beam axis. This ensures that the object remains in focus in the  $(xyz)'$  coordinate system of the STXM during raster-scanning for image acquisition. For this purpose, the sample is moved in a plane perpendicular to the axis of rotation ( $xy$ -plane of the  $xyz$  sample coordinate system in Figure 1). The scanning system axes  $(xyz)'$  are linked via the control system so as to scan parallel to the sample plane, in this manner the sample remains in focus during the scan. Thus, each sample movement in the  $x'$ -direction is accompanied by a corresponding movement the  $z'$ -direction. The same coupling is applied for the  $y'$ -direction. Depending on the experimental requirements, two detectors are available to record the trans-

mitted X-ray intensity: A photomultiplier tube (PMT), attached to an upstream phosphor screen to convert the X-rays to visible photons for normal operation, and a silicon avalanche photodiode (APD) that has the advantage of enabling the measurement of time-resolved dynamics<sup>28,29</sup> but does not provide high enough efficiency for operation in the energy range between 270 - 500 eV.

Furthermore, the laminography angle,  $\theta$ , determines the achievable depth resolution  $\Delta z$  in the direction of the axis of rotation, which can be calculated from the spatial STXM-resolution  $\Delta x$  according to<sup>23</sup>

$$\Delta z = \frac{\Delta x}{\sin \theta}. \quad (2)$$

This equation shows that the resolution along the z axis is always slightly worse than the spatial in-plane resolution achieved with the STXM. Another important parameter defined by the laminography angle is the number of required projections,  $N$ , which are a function of the sought in-plane resolution for the reconstruction,  $\Delta r$ . The number of projections for a given sample thickness  $d$  needed to guarantee enough angular sampling, is given by<sup>23</sup>

$$N \geq \pi \frac{d}{\Delta r} \tan \theta. \quad (3)$$

For computed tomography of flat samples, the accessible angular range is limited, either because the absorption gets too large or because of physical constraints in the setup. These missing angles result in a missing wedge of information in Fourier domain, which causes a decreased resolution in the direction perpendicular to the sample, and artifacts.<sup>30,31</sup> For laminography this is replaced by a more favorable missing cone of information,<sup>23</sup> which nevertheless also results in reduced resolution perpendicular to the sample plane and artifacts. The reconstruction algorithm applied here, includes an iterative refinement that uses physical constraints to estimate the missing data and reduce such artifacts.<sup>23,32,33</sup> This includes the implementation of the laminography angle, and the modified geometry compared to conventional 90° tomography. The reconstruction code is free accessible for users on request.

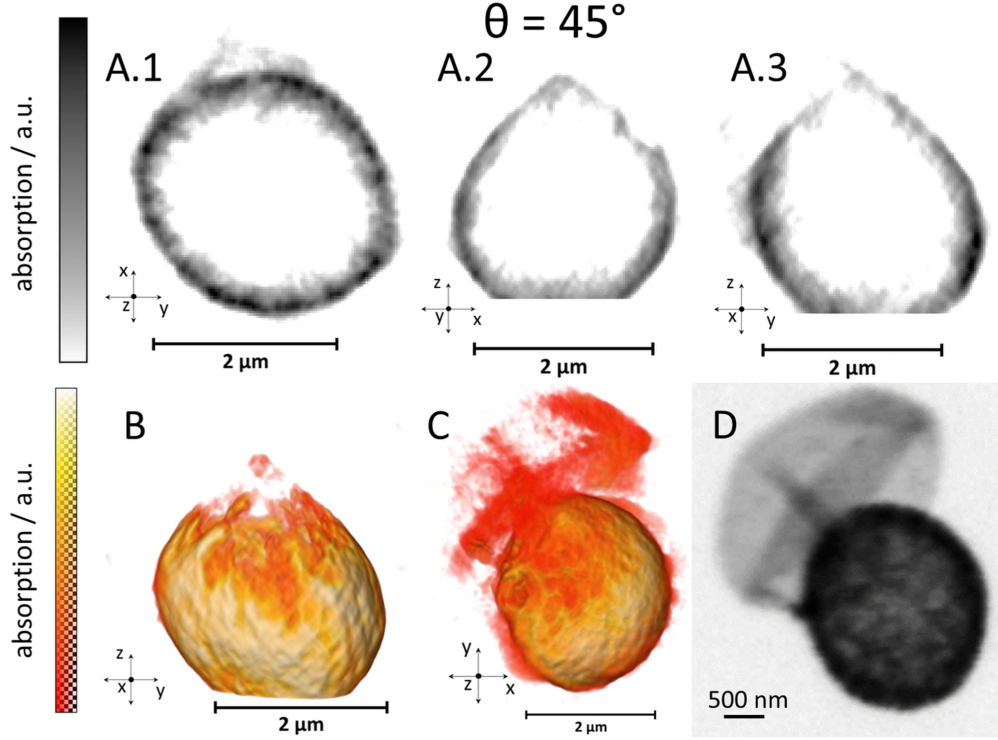


Figure 2: 3D reconstruction of an air-filled PVA-microsphere coated with magnetite NP agglomerates (*sphere 1*) at  $45^\circ$  laminographic angle. Virtual slices through the different planes show the central hollow part and the characteristic shape of the sphere (A.1-A.3). Slices parallel to the z-axis (A.2 & A.3) and the 3D volume rendering B show an exaggerated pointed tip which is caused by the missing information cone of laminography. The absorption scale bar for the volume reconstruction is the same for B and C. However, the displayed threshold in C is set to a larger value compared to B so that a collapsed PVA-balloon, which is attached to the sphere, can be seen. The deflated balloon and the SPION-coated sphere can be seen in the raw STXM projection as well (D).

All SoXL measurements presented in this work were carried out using an electroplated FZP made of gold with a diameter of  $240\ \mu\text{m}$ , a  $80\ \mu\text{m}$  central stop and  $35\ \text{nm}$  outermost zone width in combination with a  $75\ \mu\text{m}$  OSA. Further parameters and measurement specific settings are summarized in Table S1 in the SI.

In this letter, examples of applications ranging from functionalized nanomaterials, biological nanostructures with photonic properties and sophisticated nanostructured magnetic materials are shown to illustrate the wide range of research areas that can be investigated using SoXL.

Polymeric microspheres functionalized with inorganic nanoparticles (NPs) find application

in medical therapies and diagnostics, e.g. as contrast agents or for local drug release triggered by external magnetic fields,<sup>34</sup> and have been the object of previous in-depth investigations concerning their physical and chemical properties.<sup>35,36</sup> Superparamagnetic iron-oxide nanoparticles (SPIONs),<sup>37</sup> can also function as a core for different coating materials or be attached to the surface of a polymer-based sphere.<sup>36</sup> For the latter, the distribution of SPIONs is a key aspect for the way the complex interacts with biological systems.<sup>38</sup>

Here, air-filled polyvinyl acetate (PVA)-based microspheres, featuring an inhomogeneous surface coating of agglomerates of highly X-ray absorbent magnetite ( $\text{Fe}_3\text{O}_4$ ) SPIONs,<sup>27</sup> were investigated using SoXL to reveal the spatial distribution of SPIONs in 3D.

Two different microspheres with a diameter of approximately  $2\text{ }\mu\text{m}$ , were measured at both laminography angles (sphere 1:  $\theta = 45^\circ$ , Figure 2 and sphere 2:  $\theta = 60^\circ$ , Figure 3) to compare the two geometries. A field of view (FOV) of  $5 \times 5\text{ }\mu\text{m}^2$  and  $4 \times 4\text{ }\mu\text{m}^2$  (pixel size:  $25 \times 25\text{ nm}^2$ ) was chosen for sphere 1 and sphere 2, respectively. 40 projections for sphere 1 and 90 projections for sphere 2, respectively, were acquired at 711 eV for optimum absorption contrast of the iron oxide agglomerates.

The slightly larger FOV for sphere 1 was chosen to include as well an attached, collapsed microsphere without coating, as can be seen in the raw STXM projection in 2D. What cannot be easily observed from the 2D STXM image but is obvious in the 3D reconstruction, is the inhomogeneous distribution of the NP coating (Figure 2B). For this specific case, the collapsed sphere helps in two ways. On the one hand, it can be visualized in the reconstruction by suitable selection of the displayed threshold value (Figure 2C), while keeping the same absorption scale bar for the volume renderings in Figure 2B and 2C. On the other hand, due to the much lower absorption of the polymeric shell, the threshold value can be adjusted to render the polymer invisible, leaving only the magnetite agglomerates visible (Figure 2B). The slices through the different planes of the sphere provide a detailed overview about the exact shape of the sphere. The slices parallel to the z-axis (Figure 2 A.2 & A.3) also illustrate the characteristic missing cone-artifact of laminography. For round-shaped objects, this can

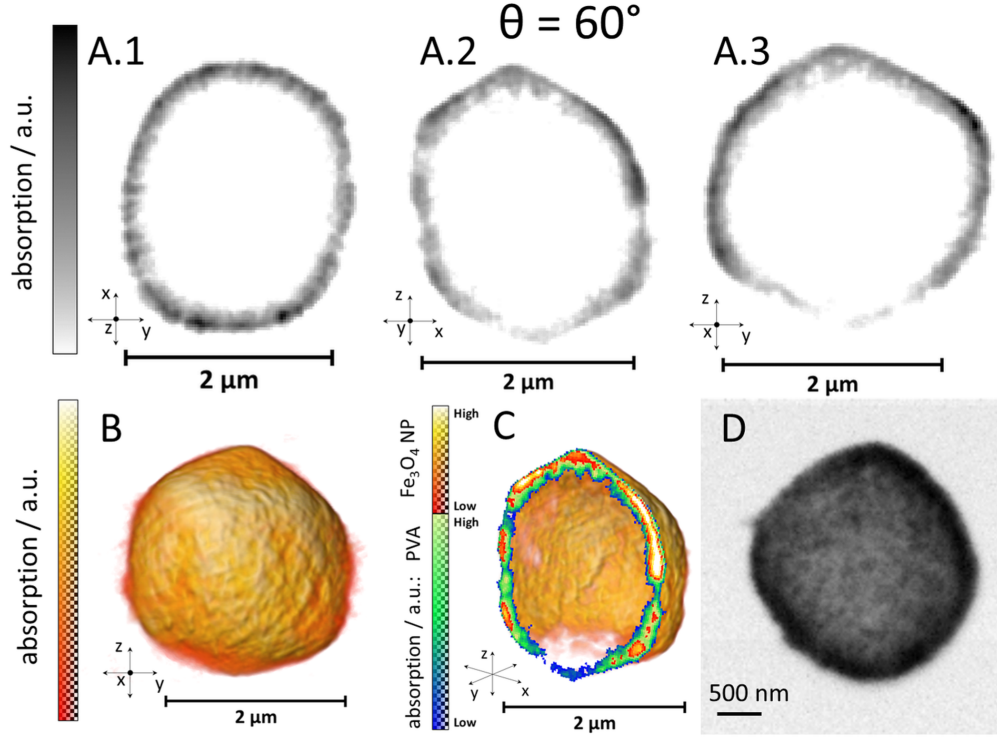


Figure 3: 3D reconstruction of an air-filled PVA-microsphere coated with magnetite NP agglomerates (*sphere 2*) using 60°-SoXL. Virtual slices (A.1-A.3) and volume renderings (B & C) illustrate the more spherical shape and a less pronounced missing cone artifact compared to sphere 1. A slice through the volume rendering (C) shows the higher resolution in z-direction for the 60° geometry, allowing a distinction between the polymeric shell (blue/green) and the magnetite agglomerates (red/white). The 3D reconstruction confirms the more uniform distribution of the iron oxide agglomerates visible in the raw STXM image (D).

result in an exaggerated pointed tip. For this artifact, the opening angle corresponds to twice the laminography angle of the respective geometry, which is about 90° for sphere 1. It is important to note that the "pointy tip"-artifact has also a certain contribution to the previous mentioned interpretation concerning the inhomogeneous distributed coating.

This artifact is less pronounced in the case of sphere 2, as can be seen in the virtual slices (Figure 3 A.2 & A.3) and the volume rendering (Figure 3B), as expected. Furthermore, the iron oxide agglomerates are more evenly distributed compared to sphere 1, which is already visible in the single projections (Figure 3D) and confirmed by the 3D reconstruction. As the beamline settings regarding the spatial resolution of the STXM (energy, FZP, exit slit

size, see Table S1) were equal for both measurements, the z-resolution (in the direction of the axis of rotation) is increased by a factor of 1.2 with 60° laminography angle. The reduced artifacts of the 60° geometry allow to apply a threshold between the polymer shell (blue/green color scale) and the iron oxide agglomerates (red/white color scale) as shown in the slice through the volume rendering in Figure 3C.

Cross sections through the spheres in the xy-plane showed a thickness for the sphere walls between 500 and 600 nm (see Figures S4 and S6 in the SI), which is in perfect agreement with previous investigations on these objects.<sup>36,38</sup> As the SPIONs exhibit an average diameter of 10 nm,<sup>36</sup> agglomerates of NPs can be resolved rather than single NPs.

Cross sections through four of these agglomerates of sphere 2 revealed diameters with full widths at half maximum (FWHM) between 76 nm and 162 nm which provide an upper bound for the achieved spatial resolution in the reconstruction of sphere 2 (see Figure S5 in the SI). According to equation 3 to ensure a transverse resolution,  $\Delta r$ , of 150 nm on an arbitrary sample of thickness  $d = 2500 \mu\text{m}$  ( $d = 2000 \mu\text{m}$ ) and laminography angle of  $\theta = 60^\circ$  ( $45^\circ$ ), is  $N = 90$  (42). However, proper angular sampling is always dependent on the actual structure to be reconstructed. Since this sample is spatially sparse, the number of needed projections can be significantly smaller than the estimate in equation 3. This resolution estimate is further supported by edge sharpness measurements shown in Figure S6 in the SI. To summarize, the SoXL 3D reconstructions of the two spheres provide detailed information about the respective object while the achieved spatial resolution below 100 nm in the x-, y-, and z-directions is sufficient to distinguish between different materials due to their absorption contrasts. In addition, the comparison shows specific properties of the available SoXL geometries at PolLux. The next example for SoXL shows a five-times larger biological specimen providing a complex nanostructure.

Well-known natural photonic crystals can be found in the colorful wings of many butterfly species, which in turn are composed of a multitude of small scales. Each butterfly wing scale (BWS) consists of a filigree and periodic three dimensional network of interconnected ridges,

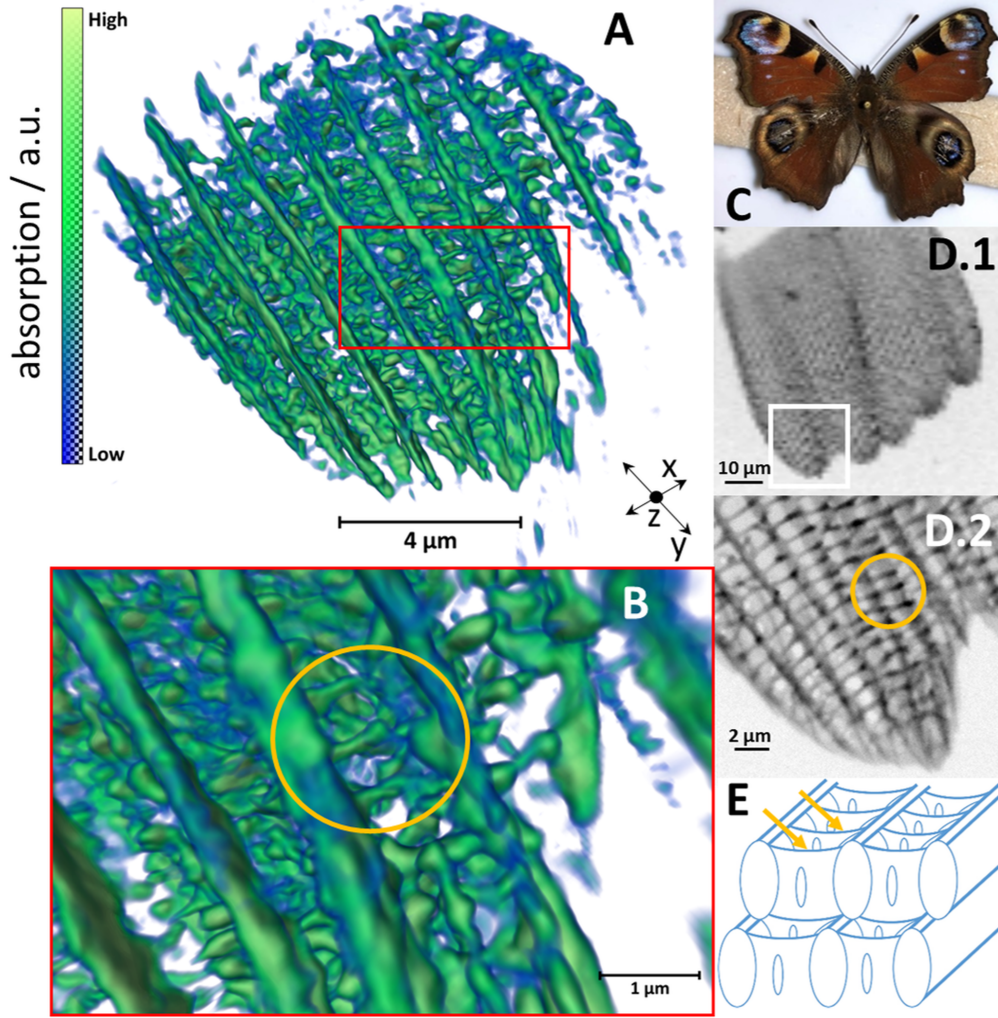


Figure 4: 3D rendering (A) of a front tip of a butterfly wing scale (BWS, raw STXM images D.1 & D.2) from a European peacock (C). A magnification into the middle part of the front tip (red rectangle), reveals a detailed view of fine crossribs that connect the ridges (B). The same crossribs can also be identified under a certain projection angle in the raw STXM image (yellow circle, B & D.2). The yellow arrows in the simplified schematic (based on<sup>39</sup>) point out where the ribs are located between the ridges (E). Virtual slices and additional volume renderings providing further insights to the internal structure of the BWS are shown in Figure S8 and S9.

(micro-)ribs and lamellae.<sup>39</sup> This specific structure, in combination with light absorbing pigments, causes strong wavelength-dependent light scattering and reflections, and creates the large variety of different colors seen for these insects.<sup>40</sup>

In this example, a BWS from a European peacock butterfly (*Aglaia io*) was selected to demonstrate the capabilities of SoXL in the field of complex, carbon-based biological struc-



tures (Figure 4). One of the front tips of the BWS was selected in a FOV of  $10 \times 10 \mu\text{m}^2$  (pixel size:  $50 \times 50 \text{ nm}^2$ ) for the SoXL measurements with a laminography angle of  $45^\circ$ . This angle was selected due to practical reasons, taken into account that a higher resolution would be achieved using the  $60^\circ$  geometry but was not necessary for the investigation of this sample. Based on a first estimate of the thickness of the front tip of about  $5 \mu\text{m}$  and in order to guarantee a real-space resolution  $\Delta r$  of  $175 \text{ nm}$ , a total of 90 projections was recorded. However, it became clear during the reconstruction process that the thickness had to be increased to  $6.5 \mu\text{m}$  to display the entire BWS tip. Instead of measuring at the Carbon K-edge ( $E = 285 \text{ eV}$ ) for optimal contrast, the higher photon energy of  $E = 711 \text{ eV}$  was chosen as a compromise between comfortable working distances during the measurements, higher photon flux and sufficient contrast of the object.

The volume rendering of the 3D reconstruction in Figure 4A shows an overview of the grid-like internal structure of the BWS tip. While the resolution towards the edges is degraded due to fewer overlapping projections for the reconstruction, a normal feature in laminography, a zoom into the inner part (red rectangle in Figure 4A) reveals a detailed view of ridges connected by crossribs (Figures 4B). These crossribs have diameters in the range of  $(150 \pm 50) \text{ nm}$  and can also be identified in some of the STXM projections (yellow circle in Figures 4B and D.2). It's important to note that for this example not the entire BWS was in the FOV, but only a small area of it. This underlines the possibility of using SoXL and laminography in general to acquire overviews and subsequently "zoom-in" on selected parts of a sample with higher resolution to obtain more detailed information.<sup>23</sup> Even though the coarse structure containing ridges and ribs can be identified in the STXM images (Figure 4 D.1 and D.2), it becomes clear from virtual slices through the 3D reconstruction that the tip has an internal curvature and that it is slightly curving upwards (see Figure S8 in the SI). The 3D visualization further shows how the different planes are connected to each other, similar to the simplified schematic depicted in Figure 4E.

In contrast to previous 2D-imaging by transmission electron microscopy of the internal struc-

ture of BWSs,<sup>39,40</sup> SoXL has the advantage of presenting the entire volume and not only the first plane of the ridges. This allows for subsequent numerical simulations, e.g. of the interaction of light with these structures. Although the spatial information of this sample is also accessible by using hard X-ray computed nano-tomography (CT),<sup>41</sup> it is noteworthy that SoXL can be sensitive to chemical bonds of light elements in organic materials, therefore providing extra insight in addition to reveal the 3D structure.

The SoXL results shown so far were mainly based on their absorption contrast. To illustrate the spectroscopic contrast of soft X-rays, the last example will reveal the increased sensitivity concerning magnetic states and magnetic contrast in case of the L-absorption edges of transition metals.

Until recently, most of the X-ray microscopy investigations of magnetic materials have been carried out with 2D methods, such as e.g. STXM,<sup>42</sup> holography,<sup>43</sup> and photoemission electron microscopy.<sup>44,45</sup> Recent developments in hard X-ray magnetization vector CT<sup>46</sup> and in the reconstruction algorithms<sup>47,48</sup> have allowed for the achievement of 3D magnetic imaging of bulk-like samples.<sup>46</sup>

However, hard X-rays are not the most efficient choice for X-ray magnetic imaging, especially for transition metal-based magnetic materials, as their K absorption-edges exhibit an extremely low X-ray magnetic circular dichroism (XMCD) asymmetry.<sup>49,50</sup> Instead, the  $L_2$  and  $L_3$  absorption edges, which find themselves in the soft X-ray energy range, exhibit XMCD asymmetries up to 20-30%,<sup>51</sup> making these energies a prime choice for the magnetic imaging of these materials. Previous work based on soft X-ray tomography has already successfully demonstrated the investigation of 3D magnetic structures but facing as well the limitations concerning the size, shape and risk of collision of conventional tomographic imaging as described above.<sup>52</sup>

Recently, laminography has been applied to three-dimensional magnetic imaging in the hard X-ray regime, demonstrating the successful reconstruction of the 3 components of the magnetization vector field with only one axis of rotation.<sup>53</sup> As a result, the development of

SoXL provides an opportunity to combine the advantages of the laminography geometry for magnetic imaging with the high XMCD signal found in the soft X-ray range. This allows for the determination of the magnetic configuration of both 3D topological structures predicted to occur in thin magnetic discs,<sup>54</sup> as well as patterned three-dimensional magnetic nanostructures, which are predicted to exhibit new curvature-induced magnetic textures and dynamical properties, making them promising candidates for future technological applications.<sup>55</sup>

To assess the performances of SoXL with respect to 3D magnetic imaging, a magnetic lamino-gram of a 150 nm thick  $\text{Ni}_{81}\text{Fe}_{19}$  (Permalloy, Py) disc with an average diameter of 835 nm at the center of the disc was performed. The thickness of the Py disc, and the growth rate of the Py were selected to allow for the development of a weak perpendicular magnetic anisotropy (PMA).<sup>56</sup> A detailed description of the disc fabrication can be found elsewhere.<sup>57</sup> An important factor in the choice of this material is that the magnetic configuration is controlled exclusively by the geometry of the disc, providing therefore a known, reproducible, but nonetheless complex spin state. This spin configuration, called "target" or  $n\pi$  state,<sup>57,58</sup> is characterized by concentric, perpendicularly magnetized ring domains with alternating orientations. The periodicity of the ring domains is comparable to (and therefore determined by) the thickness of the Py film, and the domain walls between them are of Bloch type at the center of the film with Néel closure caps of opposite chiralities at the top and bottom surfaces of the film.<sup>57-60</sup> As no anti-symmetric exchange interaction is present for this material, both signs of the Bloch wall chirality can coexist. Finally, it is noteworthy that, for the thickness of the Py film considered here, this perpendicularly magnetized state coexists with an in-plane magnetic vortex state.<sup>57</sup>

To achieve a high spatial resolution for such a thin sample, a pixel size of  $15 \times 15 \text{ nm}^2$  was chosen for a  $2 \times 2 \mu\text{m}^2$  FOV. The calculated beam spot size at the sample was about 43 nm (see SI), however, in order to oversample in the scan and in the angles and to ensure sufficient spatial resolution, a total number of projections  $N = 79$  was recorded using the

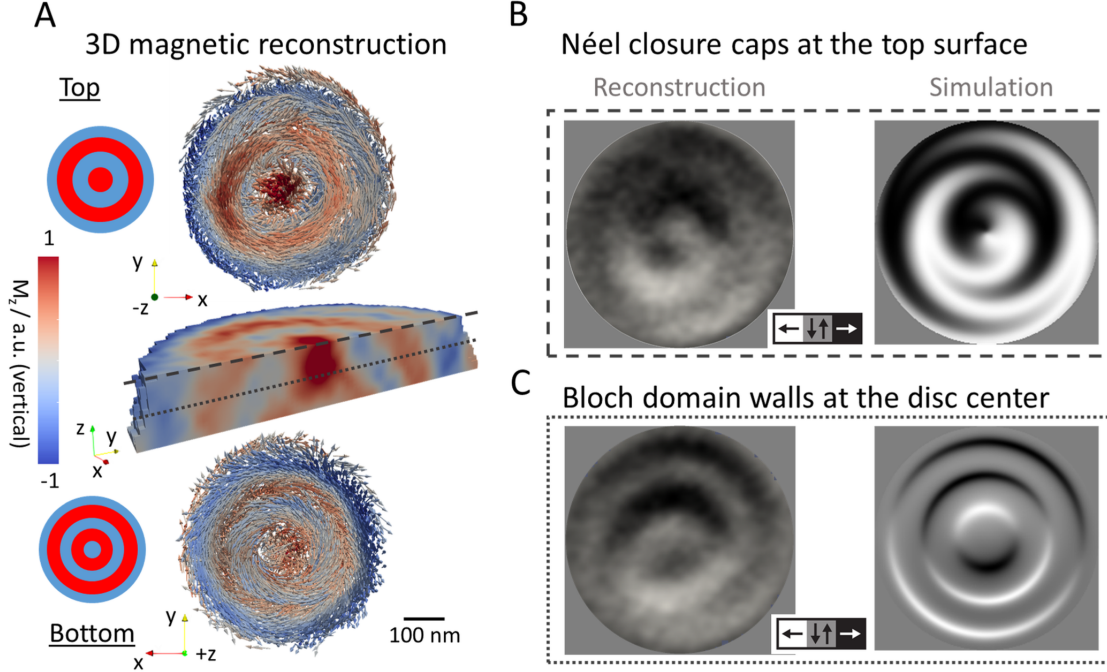


Figure 5: 3D magnetic laminography reconstruction of a 150 nm thin permalloy disc (A). The out-of-plane ( $M_z$ ) magnetic configuration features concentric perpendicularly magnetized ring domains. The cross section through the reconstructed volume illustrates a transition between two different magnetic states from top (4 ring domains) to the bottom of the disc (5 ring domains). Néel closure caps can be seen at the top surface of the disc shown in (B), which is virtual at the height shown with the dashed line in the cross section of (A). Bloch domain walls at the center of the disc can be seen in (C), which is a virtual cut at the height shown with a dotted line in the cross section of (A). The colorbar shows the in-plane magnetization direction.

$\theta = 45^\circ$  SoXL-geometry. Thereby, better statistics and signal to noise ratio in the XMCD projections and reconstruction were acquired.

To reveal the XMCD contrast of the Py disc, circularly polarized light was used to measure each projection with both polarization directions (C+ & C-) at the Fe  $L_2$  absorption edge energy at 722.8 eV. The Fe  $L_2$  edge was employed for the experiments reported here instead of the typical  $L_3$  edge. This choice was a compromise between XMCD signal and transmitted X-ray intensity.

The 3D reconstruction of the magnetic configuration in the Py disc is based on an arbitrary-projection reconstruction algorithm developed by Donnelly et al.,<sup>48,53,61</sup> which allows for the reconstruction and visualization of the in- (ip) and out-of-plane (op) components of the

local magnetization vectors. More details regarding the 3D magnetic reconstruction procedure is described in the SI. The reconstructed magnetic configuration of the Py disc is shown in Figure 5A, where it is possible to observe that the reconstructed state closely resembles the expected magnetic configuration. A perpendicularly magnetized state with a domain periodicity comparable to the thickness of the Py disc can be noticed. In addition, the complex domain walls between these perpendicularly magnetized domains could be unraveled. In particular, it is possible to monitor the presence of Néel closure caps at the top surface of the disc (Figure 5B) and of Bloch domain walls at the center of the disc (Figure 5C). Micromagnetic simulations of the same areas of the Py disc confirm these results.

Another observation that can be drawn from the SoXL study of the Py disc is the transition from a magnetic state exhibiting 4 concentric rings ( $3\pi$  state) at the top to a magnetic state exhibiting 5 concentric rings ( $4\pi$  state) at the bottom of the disc. This transition can be explained if one considers the varying diameter of the Py disc. The disc features a continuous change in its diameter along the thickness (from about  $(890 \pm 10)$  nm at the bottom to a diameter of about  $(785 \pm 10)$  nm at the top), most probably due to the heating of the resist layer during the deposition, causing slight changes in the diameter of the exposed holes. The stable magnetic configuration of these Py structures is strongly dependent on the diameter of the disc and changes in the magnetic configuration occur through a "discontinuous" change in the number of ring domains stabilized in the disc as soon as its diameter becomes larger than an integer multiple of the disc thickness.<sup>57,58</sup>

With the above discussed examples, a showcase for 3D imaging at the nanoscale using laminography in the soft X-ray regime is presented. A rotational piezo-stage has been installed into the zone plate based PolLux endstation to investigate micrometer sized objects with down to only hundreds of nm thickness. The successful reconstructions of the iron oxide functionalized microspheres, the internal network structure of a BWS and the complex magnetic orientation configuration of a Py disc illustrate the diverse application possibilities for this new branch of 3D imaging. The Py disc investigation clearly demonstrates that the

SoXL technique allows for the study of complex 3D magnetic configurations of transition metal-based ferromagnetic structures at the nanoscale. SoXL is particularly advantageous for the investigation of modern optoelectronic devices based on thin-film technologies and functional materials due to the unique interaction properties of soft X-rays with matter. In the future, FZPs with a larger focal length or specifically designed layouts better suited to a tilted sample geometry, will also enable SoXL measurements at higher resolution and/or lower energies down to the Carbon K-absorption edge, which makes SoXL an attractive tool for spectroscopic investigations of organic materials like, e.g. for photovoltaic devices. In addition, the implementation into an existing state-of-the-art STXM and the already existing expertise about time-resolved measurements<sup>29</sup> opens up new prospects to investigate dynamic processes three-dimensionally.<sup>53</sup> Another perspective is the combination of SoXL and soft X-ray ptychography, which provides the advantages of being less restricted in space due to the absence of short focal length FZPs and additionally receiving information about the phase to access both real and imaginary part of the complex transmittance. In combination with the current development of next generation synchrotron radiation sources, the total measurement time for ptychographic SoXL will furthermore decrease significantly due to the increase in photon flux provided by diffraction limited light sources.

## Acknowledgement

This project has received funding from the European Union’s Horizon 2020 research and innovation program under the Marie Skłodowska-Curie grant agreement No 701647. PolLux is funded by the BMBF (project numbers 05K16WED and 05K19WE2). The authors thank Prof. Gaio Paradossi (Università degli Studi di Roma "Tor Vergata") for providing the SPION coated microspheres. A.S. acknowledges funding by DFG grant SP 1775/1-1. C.D. was supported by the Leverhulme Trust (ECF-2018-016), the Isaac Newton Trust (18-08) and the L’Oréal-UNESCO UK and Ireland Fellowship For Women In Science.

## References

- (1) Bravin, A.; Coan, P.; Suortti, P. X-ray phase-contrast imaging: from pre-clinical applications towards clinic. *Physics in Medicine and Biology* **2013**, *58*, R1–R35.
- (2) Morigi, M. P.; Casali, F.; Bettuzzi, M.; Brancaccio, R.; D’Errico, V. Application of X-ray Computed Tomography to Cultural Heritage diagnostics. *Applied Physics A* **2010**, *100*, 653–661.
- (3) Dierolf, M.; Menzel, A.; Thibault, P.; Schneider, P.; Kewish, C. M.; Wepf, R.; Bunk, O.; Pfeiffer, F. Ptychographic X-ray computed tomography at the nanoscale. *Nature* **2010**, *467*, 436–439.
- (4) Holler, M.; Diaz, A.; Guizar-Sicairos, M.; Karvinen, P.; Faerm, E.; Haerkoenen, E.; Ritala, M.; Menzel, A.; Raabe, J.; Bunk, O. X-ray ptychographic computed tomography at 16 nm isotropic 3D resolution. *Scientific Reports* **2014**, *4*.
- (5) Vagberg, W.; Larsson, D. H.; Lei, M.; Arner, A.; Hertz, H. M. X-ray phase-contrast tomography for high-spatial-resolution zebrafish muscle imaging. *Scientific Reports* **2015**, *5*.
- (6) Lovric, G.; Mokso, R.; Schlepuetz, C. M.; Stampanoni, M. A multi-purpose imaging endstation for high-resolution micrometer-scaled sub-second tomography. *Physica Medica* **2016**, *32*, 1771–1778.
- (7) Furlan, K. P.; Larsson, E.; Diaz, A.; Holler, M.; Krekeler, T.; Ritter, M.; Petrov, A. Y.; Eich, M.; Blick, R.; Schneider, G. A.; et al, Photonic materials for high-temperature applications: Synthesis and characterization by X-ray ptychographic tomography. *Applied Materials Today* **2018**, *13*, 359–369.
- (8) Gros, M. A. L.; McDermott, G.; Cinquin, B. P.; Smith, E. A.; Do, M.; Chao, W. L.;

- Naulleau, P. P.; Larabell, C. A. Biological soft X-ray tomography on beamline 2.1 at the Advanced Light Source. *Journal of Synchrotron Radiation* **2014**, *21*, 1370–1377.
- (9) Johansson, G. A.; Tyliszczak, T.; Mitchell, G. E.; Keefe, M. H.; Hitchcock, A. P. Three-dimensional chemical imaging by scanning transmission X-ray spectromicroscopy. *Synchrotron Radiation* **2007**, *14*, 395–402.
- (10) Sorrentino, A.; Nicolas, J.; Valcarcel, R.; Chichon, F. J.; Rosanes, M.; Avila, J.; Tkachuk, A.; Irwin, J.; Ferrer, S.; Pereiro, E. MISTRAL: a transmission soft X-ray microscopy beamline for cryo nano-tomography of biological samples and magnetic domains. *Journal of Synchrotron Radiation* **2015**, *22*, 1112–1117.
- (11) Leontowich, A.; Berg, R.; Regier, C.; Taylor, D.; Wang, J.; Beauregard, D.; Geilhufe, J.; Swirsky, J.; Wu, J.; Karunakaran, C.; Hitchcock, A.; Urquhart, S. Cryo scanning transmission X-ray microscope optimized for spectrotomography. *Review of Scientific Instruments* **2018**, *89*.
- (12) Venkatakrishnan, S.; Farmand, M.; Yu, Y.-S.; Majidi, H.; Benthem, K. V.; Marchesini, S.; Shapiro, D. A.; Hexemer, A. Robust X-Ray Phase Ptycho-Tomography. *IEEE Signal Processing Letters* **2016**, *23*, 944–948.
- (13) Wu, J.; Zhu, X.; Shapiro, D.; Lee, J.; van Buuren, T.; Biener, M.; Gammon, S.; Li, T.; Baumann, T.; Hitchcock, A. 4D imaging of ZnO coated alumina aerogels by scanning transmission X-ray microscopy and ptychographic tomography. *Journal of Physical Chemistry C* **2018**, *122*, 25374 – 25385.
- (14) Hitchcock, A. P.; Johansson, G. A.; Mitchell, G. E.; Keefe, M. H.; Tyliszczak, T. 3d chemical imaging using angle-scan nanotomography in a soft X-ray scanning transmission X-ray microscope. *Applied Physics A* **2008**, *92*, 447–452.
- (15) Wu, J.; Hitchcock, A.; Lerotic, M.; Shapiro, D.; Berejnov, V.; Susac, D.; Stumper, J.



- 4d imaging of polymer electrolyte membrane fuel cell cathodes by scanning x-ray microscopy. *Microscopy and Microanalysis S1* **2017**, *23*, 1784–1785.
- (16) Yu, Y.-S.; Farmand, M.; Kim, C.; Liu, Y.; Grey, C.; Strobridge, F.; Tyliczszak, T.; Celestre, R.; Denes, P.; Joseph, J.; et al, Three-dimensional localization of nanoscale battery reactions using soft X-ray tomography. *Nature Communications* **2018**, *9*, 921.
- (17) Wu, J.; Melo, L.; Zhu, X.; West, M.; Berejnov, V.; Susac, D.; Stumper, J.; Hitchcock, A. 4d imaging of polymer electrolyte membrane fuel cell catalyst layers by soft X-ray spectro-tomography. *Journal of Power Sources* **2018**, *381*, 72–83.
- (18) Ekam, A. A.; Chen, J.-H.; Guo, J.; McDermott, G.; Gros, M. A. L.; Larabell, C. A. Mesoscale imaging with cryo-light and X-rays: Larger than molecular machines, smaller than a cell. *Biology of the Cell* **2017**, *109*, 24–38.
- (19) Groen, J.; Conesa, J. J.; Valcarcel, R.; Pereiro, E. The cellular landscape by cryo soft X-ray tomography. *Biophysical Reviews* **2019**, *11*, 611–619.
- (20) Helfen, L.; Baumbach, T.; Mikulik, P.; Kiel, D.; Pernot, P.; Cloetens, P.; Baruchel, J. High-resolution three dimensional imaging of flat objects by synchrotron-radiation computed laminography. *Applied Physics Letters* **2005**, *86*, 071915.
- (21) Helfen, L.; Myagotin, A.; Rack, A.; Pernot, P.; and M. Di Michiel, P. M.; Baumbach, T. Synchrotron-radiation computed laminography for high-resolution three-dimensional imaging of flat devices. *Physica Status Solidi A - Applications and Materials Science* **2007**, *204*, 2760–2765.
- (22) Helfen, L.; Myagotin, A.; Mikulik, P.; Pernot, P.; Voropaev, A.; Elyyan, M.; Michiel, M. D.; Baruchel, J.; Baumbach, T. On the implementation of computed laminography using synchrotron radiation. *Review of Scientific Instruments* **2011**, *82*, 063702.

- (23) Holler, M.; Odstrcil, M.; Guizar-Sicairos, M.; Lebugle, M.; Mueller, E.; Finizio, S.; Tinti, G.; David, C.; Zusman, J.; Unglaub, W.; et al, Three-dimensional imaging of integrated circuits with macro- to nanoscale zoom. *Nature Electronics* **2019**, *2*, 464–470.
- (24) Flechsig, U.; Quitmann, C.; Raabe, J.; Boege, M.; Fink, R. H.; Ade, H. The PolLux Microspectroscopy Beamline at the Swiss Light Source. *AIP Conference Proceedings* **2006**, *879*, 505–508.
- (25) Raabe, J.; Tzvetkov, G.; Flechsig, U.; Boege, M.; Jaggi, A.; Sarafimov, B.; Vernooij, M. G.; Huthwelker, T.; Ade, H.; Kilcoyne, D.; et al, PolLux: a new facility for soft X-ray spectromicroscopy at the Swiss Light Source. *Review of Scientific Instruments* **2008**, *79*, 113704.
- (26) Roesner, B.; Koch, F.; Doehring, F.; Bosgra, J.; Guzenko, V. A.; Kirk, E.; Meyer, M.; Ornelas, J. L.; Fink, R. H.; Stanescu, S.; et al, Exploiting atomic layer deposition for fabricating sub-10 nm X-ray lenses. *Microelectronic Engineering* **2018**, *191*, 91–96.
- (27) Spaeth, A.; Schoell, S.; Riess, C.; Schmidtel, D.; Paradossi, G.; Raabe, J.; Horneegger, J.; Fink, R. H. STXM goes 3D: Digital reconstruction of focal stacks as novel approach towards confocal soft x-ray microscopy. *Ultramicroscopy* **2014**, *144*, 19–25.
- (28) Puzic, A.; Korhonen, T.; Kalantari, B.; Raabe, J.; Quitmann, C.; Juellig, P.; Bommer, L.; Goll, D.; Schuetz, G.; Wintz, S.; et al, Photon Counting System for Time-resolved Experiments in Multibunch Mode. *Synchrotron Radiation News* **2010**, *23*, 26–32.
- (29) Finizio, S.; Wintz, S.; Watts, B.; Raabe, J. Sub-100ps Magnetic Imaging at the PolLux Endstation of the Swiss Light Source. *Microscopy and Microanalysis* **2018**, *24*, 452–453.
- (30) Turonova, B.; Marsalek, L.; Slusallek, P. On geometric artifacts in cryo electron tomography. *Ultramicroscopy* **2016**, *163*, 48–61.

- (31) Bals, S.; Goris, B.; Altantzis, T.; Heidari, H.; Aert, S. V.; Tendeloo, G. V. Seeing and measuring in 3D with electrons. *Comptes Rendus Physique* **2014**, *15*, 140–150.
- (32) Guizar-Sicairos, M.; Diaz, A.; Holler, M.; Lucas, M. S.; Menzel, A.; Wepf, R. A.; Bunk, O. Phase tomography from x-ray coherent diffractive imaging projections. *Opt. Express* **2011**, *19*, 21345–21357.
- (33) Guizar-Sicairos, M.; Boon, J. J.; Mader, K.; Diaz, A.; Menzel, A.; Bunk, O. Quantitative interior X-ray nanotomography by a hybrid imaging technique. *Optica* **2015**, *2*, 259–266.
- (34) Lentacker, I.; Smedt, S. C. D.; Sanders, N. N. Drug loaded microbubbles design for ultrasound triggered delivery. *Soft Matter* **2009**, *5*, 2161–2170.
- (35) Tzvetkov, G.; Graf, B.; Fernandes, P.; Frey, A.; Cavalieri, F.; Paradossi, G.; Fink, R. H. In situ characterization of gas-filled microballoons using soft X-ray microspectroscopy. *Soft Matter* **2008**, *4*, 510–514.
- (36) Brismar, T. B.; Grishenkov, D.; Gustafsson, B.; Haermark, J.; Barrefelt, A.; Kothapalli, S. V. V. N.; Margheritelli, S.; Oddo, L.; Caidahl, K.; Hebert, H.; et al, Magnetite nanoparticles can be coupled to microbubbles to support multimodal imaging. *Biomacromolecules* **2012**, *13*, 1390–1399.
- (37) Palanisamy, S.; Wang, Y. M. Superparamagnetic iron oxide nanoparticulate system: synthesis, targeting, drug delivery and therapy in cancer. *Dalton Transactions* **2019**, *48*, 9490–9515.
- (38) Ahmed, M.; Cerroni, B.; Razuvaev, A.; Haermark, J.; Paradossi, G.; Caidahl, K.; Gustafsson, B. Cellular Uptake of Plain and SPION-Modified Microbubbles for Potential Use in Molecular Imaging. *Cellular and Molecular Bioengineering* **2017**, *10*, 537–548.

- (39) Ghiradella, H. Insect Cuticular Surface Modifications: Scales and Other Structural Formations. *Advances in Insect Physiology* **2010**, *38*, 135–180.
- (40) Stavenga, D. G.; Leertouwer, H. L.; Wilts, B. D. Coloration principles of nymphaline butterflies - thin films, melanin, ommochromes and wing scale stacking. *Journal of Experimental Biology* **2014**, *217*, 2171–2180.
- (41) Wilts, B. D.; Sheng, X.; Holler, M.; Diaz, A.; Guizar-Sicairos, M.; Hoppe, R.; Liu, S. H.; Langford, R.; Onelli, O. D.; Chen, D.; et al, Evolutionary-Optimized Photonic Network Structure in White Beetle Wing Scales. *Advanced Materials* **2018**, *30*, 1702057.
- (42) Wintz, S.; Strache, T.; Koerner, M.; Bunce, C.; ; Banholzer, A.; Moench, I.; Mattheis, R.; Raabe, J.; Quitmann, C.; McCord, J.; et al, Control of vortex pair states by post-deposition interlayer exchange coupling modification. *Physical Review B* **2012**, *85*, 134417.
- (43) Eisebitt, S.; Luening, J.; Schlotter, W. F.; Loering, M.; Hellwig, O.; Eberhardt, W.; Stoehr, J. Lensless imaging of magnetic nanostructures by X-ray spectro-holography. *Nature* **2004**, *432*, 885–888.
- (44) Guyader, L. L.; Savoini, M.; Moussaoui, S. E.; Buzzi, M.; Tuskamoto, A.; Itoh, A.; Kirilyuk, A.; Rasing, T.; Kimel, A. V.; Nolting, F. Nanoscale sub-100 picosecond all-optical magnetization switching in GdFeCo microstructures. *Nature Communications* **2015**, *6*, 5839.
- (45) Boule, O.; Vogel, J.; Yang, H. X.; Pizzini, S.; Chaves, D. D.; Locatelli, A.; Mentès, T. O.; Sala, S.; Buda-Preijbeanu, L. D.; Klein, O.; et al, Room-temperature chiral magnetic skyrmions in ultrathin magnetic nanostructures. *Nature Nanotechnologies* **2016**, *11*, 449–454.
- (46) Donnelly, C.; Guizar-Sicairos, M.; Scagnoli, V.; Gliga, S.; Holler, M.; Raabe, J.; Hey-

- derman, L. J. Three-dimensional magnetization structures revealed with X-ray vector nanotomography. *Nature* **2017**, *547*, 328–331.
- (47) Hierro-Rodriguez, A.; Guersoy, D.; Phatak, C.; Quiros, C.; Sorrentino, A.; Alvarez-Prado, L. M.; Velez, M.; Martin, J. I.; Alameda, J. M.; Pereiro, E.; et al, 3D reconstruction of magnetization from dichroic soft X-ray transmission tomography. *Journal of Synchrotron Radiation* **2018**, *25*, 1144–1152.
- (48) Donnelly, C.; Gliga, S.; Scagnoli, V.; Holler, M.; Raabe, J.; Heyderman, L. J.; Guizar-Sicairos, M. Tomographic reconstruction of a three-dimensional magnetization vector field. *New Journal of Physics* **2018**, *20*, 083009.
- (49) Schuetz, G.; Wagner, W.; Wilhelm, W.; Kienle, P.; Zeller, R.; Frahm, R.; Materlik, G. Absorption of circular polarized X-rays in iron. *Physical Review Letters* **1987**, *58*, 737–740.
- (50) Donnelly, C.; Scagnoli, V.; Guizar-Sicairos, M.; Holler, M.; Wilhelm, F.; Guillou, F.; Rogalev, A.; Detlefs, C.; Menzel, A.; Raabe, J.; et al, High-resolution hard X-ray magnetic imaging with dichroic ptychography. *Physical Review B* **2016**, *94*, 064421.
- (51) Stoehr, J. X-ray magnetic circular dichroism spectroscopy of transition metal thin films. *Journal of Electron Spectroscopy and Related Phenomena* **1995**, *75*, 253–272.
- (52) Streubel, R.; Kronast, F.; Fischer, P.; Parkinson, D.; Schmidt, O.; Makarov, D. Retrieving spin textures on curved magnetic thin films with full-field soft X-ray microscopies. *Nature Communications* **2017**, *6*.
- (53) Donnelly, C.; Finizio, S.; Gliga, S.; Holler, M.; Hrabec, A.; Odstrcil, M.; Mayr, S.; Scagnoli, V.; Heyderman, L.; Guizar-Sicairos, M.; et al, Imaging three dimensional magnetization dynamics with laminography. *under review* **2019**,

- (54) Liu, Y. Z.; Lake, R. K.; Zang, J. D. Binding a hopfion in a chiral magnet nanodisk. *Physical Review B* **2018**, *98*, 174437.
- (55) Fernandez-Pacheco, A.; Streubel, R.; Fruchart, O.; Hertel, R.; Fischer, P.; Cowburn, R. P. Three-dimensional nanomagnetism. *Nature Communications* **2017**, *8*.
- (56) Saito, N.; Fujiwara, H.; Sugita, Y. A new type of magnetic domain structure in negative magnetostriction Ni-Fe films. *Journal of the Physical Society of Japan* **1964**, *19*, 1116–1125.
- (57) Finizio, S.; Wintz, S.; Bracher, D.; Kirk, E.; Semisalova, A. S.; Foerster, J.; Zeissler, K.; Wessels, T.; Weigand, M.; Lenz, K.; et al., Thick permalloy films for the imaging of spin texture dynamics in perpendicularly magnetized system. *Physical Review B* **2018**, *98*, 104415.
- (58) Eames, P.; Dahlberg, E. D. Characterization of domain states in submicron sized permalloy particles with perpendicular anisotropy. *Journal of Applied Physics* **2002**, *91*, 7986–7988.
- (59) Moutafis, C.; Komineas, S.; Vaz, C. A. F.; Bland, J. A. C.; Eames, P. Vortices in ferromagnetic elements with perpendicular anisotropy. *Physical Review B* **2006**, *74*, 214406.
- (60) Komineas, S.; Vaz, C. A. F.; Bland, J. A. C.; Papanicolaou, N. Bubble domains in disc-shaped ferromagnetic particles. *Physical Review B* **2005**, *71*, 060405.
- (61) Donnelly, C.; Guizar-Sicairos, M. Magnetic tomography reconstruction algorithm. 2018; <https://zenodo.org/record/1319763>.

## For Table of Contents Only

